NASA TECHNICAL NOTE

DIMPLE, SPALL, AND PERFORATION CHARACTERISTICS OF THIN PLATES OF NINE MATERIALS UNDER HYPERVELOCITY IMPACT

by Nestor Clough, Seymour Lieblein, and Allen R. McMillan

Lewis Research Center
Cleveland, Ohio

1. Report No. NASA TN D-5625	2. Government Accession No.	3. Recipient's Catalog No.
4. Title and Subtitle DIMPLE, SPALL, AND PERFORATION CHARACTERISTICS OF THIN PLATES OF NINE MATERIALS UNDER HYPERVELOCITY IMPACT		5. Report Date January 1970
		6. Performing Organization Code
7. Author(s) Nestor Clough, Seymour Lieblein, Lewis Research Center; and Allen R. McMillan, General Motors, Warren, Mich.		8. Performing Organization Report No. E-4966
9. Performing Organization Name and Address Lewis Research Center National Aeronautics and Space Administration Cleveland, Ohio 44135		10. Work Unit No. 120-27
		11. Contract or Grant No.
12. Sponsoring Agency Name and Address National Aeronautics and Space Administration Washington, D.C. 20546		13. Type of Report and Period Covered Technical Note
		14. Sponsoring Agency Code

15. Supplementary Notes

16. Abstract

Spherical projectiles of approximately 0.018 gram mass were accelerated to a velocity of approximately 7.6 km/sec and impacted against flat-plate targets of varying thickness in an evacuated chamber. Variations in target temperature and projectile density were included. Target thicknesses at incipient perforation and at rear-surface dimple and spall were determined for nine materials. Thickness ratios at the onset of each of the damage modes, and the corresponding mass of armor required, varied significantly with target material and temperature and with projectile material. A correlation was proposed for the variation of ratio of target thickness at perforation to projectile diameter which included the effects of projectile density and target temperature.

17. Key Words (Suggested by Author(s)) Hypervelocity impact	18. Distribution Statement Unclassified - unlimited		
19. Security Classif. (of this report) Unclassified	20. Security Classif. (of this page) Unclassified	21. No. of Pages 34	22. Price* $3.00

*For sale by the Clearinghouse for Federal Scientific and Technical Information Springfield, Virginia 22151

DIMPLE, SPALL, AND PERFORATION CHARACTERISTICS OF THIN

PLATES OF NINE MATERIALS UNDER HYPERVELOCITY IMPACT

by Nestor Clough, Seymour Lieblein, and Allen R. McMillan[*]

Lewis Research Center

SUMMARY

An experimental research program was conducted to determine the critical damage modes that might be inflicted on various armor materials by the impact of a high-velocity projectile. The experimental program was performed under NASA contract on a ballistics range facility of the General Motors Corporation, Defense Research Laboratories, Santa Barbara, California. Spherical projectiles of approximately 0.018 gram mass were accelerated to a velocity of approximately 7.6 kilometers per second and impacted against flat-plate targets of varying thickness in an evacuated chamber. The projectiles used included 0.238-centimeter-diameter pyrex (density, 2.26 g/cm^3), 0.318-centimeter-diameter nylon (density, 1.035 g/cm^3), and 0.368-centimeter-diameter Inlyte (density, 0.745 g/cm^3). Target thickness at incipient perforation and at rear-surface dimple and spall were determined for plates of L-605, Inconel-718, and A-286 at room temperature, AISI 316 stainless steel and vanadium at 977 K, molybdenum-TZM at 1365 K, 2024-T6 aluminum at 644 K, titanium - 6-aluminum - 4-vanadium at 699 K, and stainless-steel-clad copper at 949 K.

The data were expressed in terms of the ratio of the target thickness at a given damage mode to the crater depth in a thick section of the same material, and the corresponding ratio of target thickness to projectile diameter. The results indicated that the target thickness ratios at the onset of each of the damage modes varied significantly with target material and temperature, and with projectile material. Comparable variations in the mass of plate armor corresponding to the incipient damage modes were also indicated, with titanium, aluminum, and vanadium providing the lowest mass values. With the inclusion of a projectile density effect established from the data, the variation of ratio of target thickness at perforation to projectile diameter agreed with a previously determined correlating parameter for targets at room temperature. A tentative relation was proposed for prediction of target thickness at perforation for elevated temperatures.

---

*Senior Research Physicist, Warren Research Laboratory, General Motors Corporation, Warren, Michigan.

INTRODUCTION

The existence of a hazard to space vehicle components from the impact of meteoroids has been recognized as an important factor in the design of such components. An analysis of the meteoroid damage problem for waste-heat radiators of space power systems is presented in reference 1. There, it is pointed out that the evaluation of the total hazard is a function of two separate factors: first, definition of the meteoroid population in terms of relative impact velocity, rate of meteoroid impact, and meteoroid structure; and second, an understanding of the phenomenon of hypervelocity impact. Problems associated with the definition of the first of these two areas are discussed in reference 2.

The general characteristics of the craters resulting from hypervelocity impact into thick plates of various materials can be obtained, for example, from references 3 to 5. More recent results of impacts into thick plates of a large number of materials for which target temperature and projectile density were varied are presented in reference 6. However, little information exists describing the specific damage likely to be incurred by the vulnerable portions of space vehicle components under operational conditions.

For the waste-heat radiators of space vehicles, the required armor thickness for the fluid-carrying tubes is generally determined by multiplying the calculated thick-plate crater depth that would result from the impact (e.g., as obtained from ref. 6) by an arbitrary factor (ref. 1). The factor is to be determined for the type of damage judged to be critical to the operation of the radiator. From the initial results of impacts into tubular target configurations typical of space waste-heat radiators reported in reference 7, it was established that damage modes other than complete perforation of the radiator tube exist that may be critical to the successful operation of the radiator. In particular, it was shown that the inner surface of a tube could dimple and spall with armor thicknesses significantly greater than the crater depth. It was necessary therefore to study the effects of pertinent variables on inner-surface dimple, spall, and perforation, and to establish appropriate relations for predicting the required armor thickness.

Reference 8 gives the results of an investigation in which the limits of dimple, spall, and perforation were defined for flat plates of 316 stainless steel, 2024-T6 aluminum, and columbium - 1-percent zirconium impacted at room temperature by pyrex projectiles. The target thickness at incipient dimple, spall, and perforation varied widely for each material. In view of these results, it was desirable to conduct further impacts into a wider range of potential armor materials and to include the effects of target temperature and projectile properties on target damage characteristics.

Reported herein are the results of an experimental hypervelocity-impact program in which flat-plate targets of nine materials were impacted with projectiles of nominally constant mass and velocity, but with three different values of density. The plate thickness was varied so that the threshold limits of perforation, spall, and dimple could be defined. The targets tested consisted of flat plates of L-605, Inconel-718, and A-286 at room temperature, AISI 316 stainless steel and vanadium at 977 K, molybdenum-TZM at 1365 K, 2024-T6 aluminum at 644 K, titanium alloy at 699 K, and stainless-steel-clad copper at 949 K. These targets were impacted at a nominal velocity of 7.6 kilometers per second with spherical projectiles of 0.015 to 0.020 gram mass. The experimental program was conducted at the General Motors Corporation, Defense Research Laboratory, Santa Barbara, California under NASA contract.

SYMBOLS

d	projectile diameter, cm
E_t	Young's modulus of elasticity for target, dyne/cm^2
K, K_1, K_2	constants
M'	armor mass parameter, $\rho_t(t^*/d)$, g/cm^3
m	projectile mass, g
m^*	reference projectile mass, g
P	measured penetration depth in target, cm
P_∞	penetration depth in thick (semi-infinite) target, cm
P_∞^*	reference penetration depth in thickest target within series, cm
T	temperature, K
t	target thickness, cm
t^*	target thickness at incipient rear-surface damage, cm
t^*/P_∞	damage thickness factor
V	projectile velocity, km/sec
V^*	reference projectile velocity, km/sec
γ	material cratering coefficient
ϵ_t	elongation of target material (5.08-cm specimen), percent

ρ_p projectile density, g/cm^3

ρ_t target density, g/cm^3

Subscripts:

R room temperature

T elevated temperature

TESTS

All tests were conducted on a ballistics range that is fully described in reference 9. The range and apparatus used were the same as used for the programs reported in references 6 to 8. The basic equipment consists of a 30-caliber accelerated-reservoir light-gas gun, a 6-meter free-flight range, and an evacuted impact chamber. The target materials tested were L-605, Inconel-718, A-286, 316 stainless steel, Ti-6Al-4V, molybdenum-TZM, commercially pure cast vanadium, 2024-T6 aluminum, and stainless-steel-clad copper. All materials except the clad copper were obtained as bars, nominally 10 centimeters square. The targets were cut from these bars in varying thicknesses as required. Stainless-steel-clad-copper targets were fabricated in various thicknesses from oxygen-free high-conductivity copper and 316 stainless-steel plates by use of a commercially available braze alloy. Two target designs of the same total thickness were employed; the first had 0.0456-centimeter-thick 316-stainless-steel cladding on both sides of the copper, and the second used 0.094-centimeter stainless. The total thickness of the targets was varied by varying the copper core thickness in these steps for each design, while maintaining the same total thickness for both designs in each step.

The experimental procedure involved impacting flat-plate targets having progressively less thickness until complete perforation of the target was visible. The targets were then sectioned at the point of maximum crater depth and examined. Generally, each target material required five to nine impacts each at a different thickness to define the regimes of dimple, spall, and perforation. However, for the stainless-steel-clad copper, the thicknesses of the targets were chosen to bracket only the perforation mode. The targets were impacted at room or elevated temperatures with either a 0.238-centimeter-diameter spherical pyrex projectile (ρ_p = 2.26 g/cm^3), a 0.318-centimeter-diameter spherical nylon projectile (ρ_p = 1.035 g/cm^3), or a 0.368-centimeter-diameter spherical Inlyte projectile (ρ_p = 0.745 g/cm^3), all with masses nominally of 0.018 gram at a velocity in the range from 7.0 to 7.9 kilometers per second. A listing of the target-projectile combinations and target temperature at impact is given in table I.

TABLE I. - IMPACT TEST VARIABLES

[Impact velocity (nominally constant), 7.0 to 7.9 km/sec.]

Target material	Projectile			Target temperature, K
	Material	Diameter, cm	Density, g/cm^3	
316 Stainless steel	Pyrex	0.238	2.26	977
316 Stainless steel	Nylon	.318	1.035	[a]≈294
316 Stainless steel	Inlyte	.368	.745	
L-605	Pyrex	.238	2.26	
A-286				
Inconel-718				
Vanadium				977
Molybdenum-TZM				1365
2024-T6 aluminum				644
Titanium - 6-aluminum - 4-vanadium				699
Stainless-steel-clad copper				949

[a]Room temperature.

RESULTS AND DISCUSSION

Target Damage

In addition to measurements of the penetration or crater depth P, the type of rear-surface damage was noted. Definitions of the damage modes of interest, as they are used herein, are shown in figure 1. Dimple is defined as any measurable displacement or bulging of the free surface below the crater without dislodgement of material. A dimpling of the inner surface of a radiator tube can result in a restriction of the flow. Spall is defined as the condition that results in a breaking away of fragments of the rear surface of the target below the crater. In a fluid circuit in zero-gravity operation, such metal particles can cause serious damage to the rotating components. Perforation is used in the conventional sense of a visible puncture through which working fluid can leak and escape. In these tests, the objective was to define the points of incipient rear-surface damage; hence, the degree of dimple, spall, or perforation was estimated and reported. Visual observations of the sectioned targets were used to classify the degree of damage.

A complete tabulation of all the shots fired in conjunction with this investigation is given in table II. The table includes a description of the targets impacted, target temperature, projectile mass, velocity, and material, and measured penetration depth P.
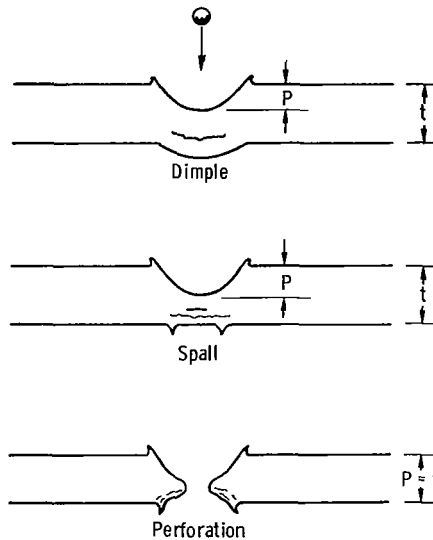
Figure 1. - Definition of damage modes.

When perforation occurred, the penetration depth was taken equal to the target thickness. Also included in the table is the qualitative description of the rear-surface damage sustained by the targets and some values used later in determining damage thickness factors.

Sectioned targets after impact are shown for each material in figure 2. The figure clearly depicts the transition from simple penetration to bulging and dimpling and finally to perforation with varying degrees of spall between these limits. It is clear from these photographs that the damage incurred in a high-velocity impact into thin plates can be greatly extended beyond that of a simple crater formation.

Damage Thickness Factors

Data presentation. - From examination of the sectioned targets of figure 2, it was possible to estimate the thickness corresponding to the onset of perforation, spall, and dimple for the particular energy level of the series of impacts and to express each thickness as a dimensionless parameter. The parameter is termed the damage thickness factor and is defined as the ratio of target thickness at incipient dimple, spall, or perforation to the semi-infinite penetration depth P_∞ in that target (that value of penetration that would have occurred in a very thick plate under identical impact conditions). The normalized target thickness t/P_∞ is useful for damage prediction relations since the ratio of target thickness to projectile diameter t/d can be obtained directly from multiplication by the ratio P_∞/d. The values of P_∞/d for a given impact condition
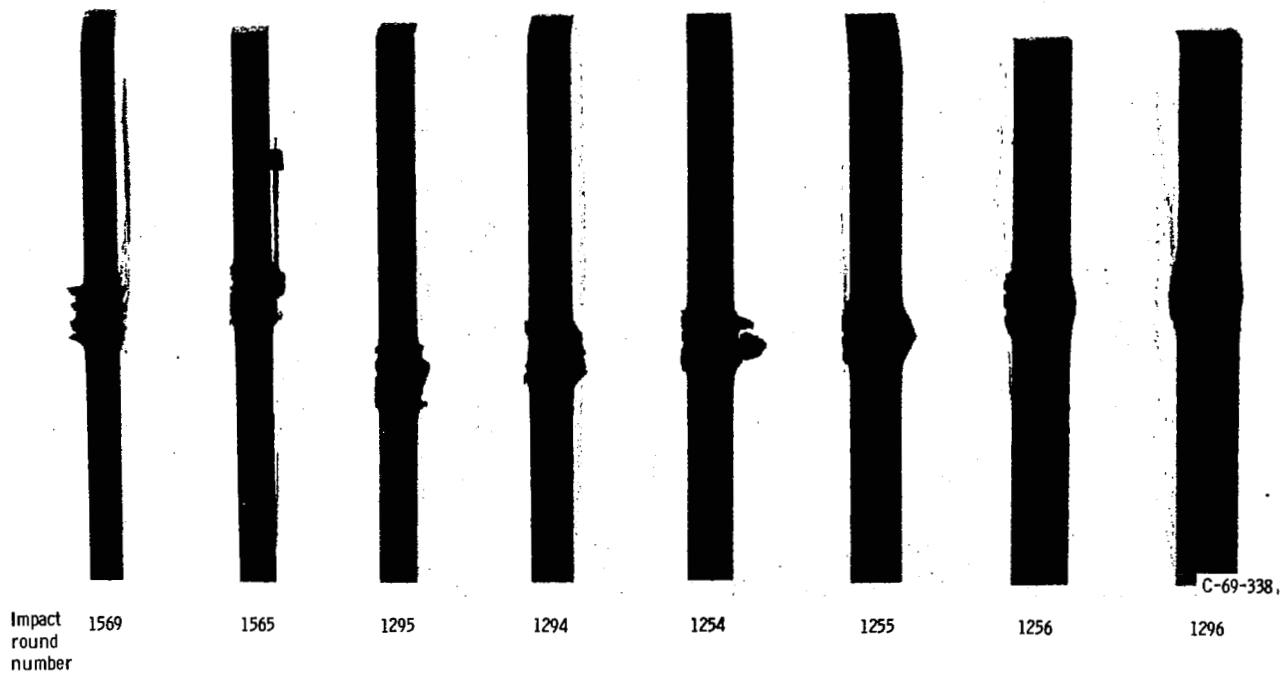
TABLE II. - ORIGINAL AND REDUCED IMPACT DATA

| Impact round number	Target			Projectile			Penetration depth, P, cm	Reference semi-infinite penetration depth, P_∞^*, cm	Calculated semi-infinite penetration depth, P_∞, cm	Rear-surface damage	Ratio, t/P_∞
	Material	Thickness, t, cm	Temperature, K	Material	Mass, m, g	Velocity, V, km/sec					
1569	Inconel-718	0.439	a294	Pyrex	0.0161	7.38	0.439	0.272	0.259	Perforation	1.70
1565		.472			.0168	7.33	.432		.262	Spall	1.81
1295		.490			.0176	7.54	.340		.271	Spall	1.81
1294		.546			.0177	7.56	.279		.272	Slight spall	2.01
1254		.584			.0179	7.33	.277		.272	Slight spall	2.15
1255		.668			.0183	7.54	.277		.274	Slight spall	2.44
1256		.741			.0180	7.61	.330		.274	Dimple	2.70
1296	↓	.800			.0177	7.56	.272	↓	.272	Slight dimple	2.94
1251	L-605	.462			.0180	7.35	.462	.234	.239	Perforation	1.93
1250		.518			.0181	7.38	.297		.240	Spall	2.16
1252		.589			.0176	7.41	.264		.239	Slight spall	2.47
1253		.645			.0178	7.16	.234		.234	Dimple	2.76
1293		.694			.0177	7.60	b.289		.243	Dimple	2.86
192	↓	1.07			.0411	7.11	.305	↓	.306	None	3.50
1292	A-286	.473			.0172	7.62	.473	.304	.306	Perforation	1.60
1291		.516			.0173	7.44	.340		.303	Spall	1.78
1261		.554			.0181	7.53	.338		.309	Slight spall	1.86
1257		.584			.0183	7.62	.340		.312	Slight spall	1.95
1266	↓	.742	↓		.0174	7.48	.304	↓	.304	Dimple	2.64
1592	2024-T6 Aluminum	.925	644		.0154	7.42	.925	.637	.615	Perforation	1.45
1593		.990			.0156	7.61	.990		.623	Perforation	1.53
1594		1.12			.0165	7.38	.694		.625	Spall	1.73
1595		1.25			.0165	7.26	.665		.620	Spall	1.95
1596		1.32			.0165	7.50	.658		.632	Slight spall	2.01
1660		1.41			.0152	7.53	.655		.617	Dimple	2.36
1658		1.59			.0155	7.29	.596		.612	None	2.59
1620		1.90			.0163	7.38	.571		.625	None	3.05
1619	↓	2.16	↓		.0168	7.53	.637	↓	.637	None	3.39
1598	316 Stainless steel	.483	977		.0166	7.49	.483	.356	.356	Perforation	1.36
1597		.534			.0164	7.40	.442		.353	Spall	1.51
1599		.610			.0162	7.50	.394		.353	↓	1.73
1600		.711			.0164	7.50	.368		.356		2.00
1601		.761			.0167	7.41	.312		.353	↓	2.16
1618		.825			.0155	7.32	.350		.343	Dimple	2.40
1659		1.018			.0151	7.53	.353		.346	Slight dimple	2.94
1617		1.08			.0162	7.50	.353		.353	None	3.06
1616	↓	1.21	↓	↓	.0165	7.50	.356	↓	.356	None	3.40

aRoom temperature.

bConsidered bad data point for determination of P_∞^*.

TABLE II. - Concluded. ORIGINAL AND REDUCED IMPACT DATA

| Impact round number	Target		Projectile				Penetration depth, P, cm	Reference semi-infinite penetration depth, P_∞^*, cm	Calculated semi-infinite penetration depth, P_∞, cm	Rear-surface damage	Ratio, t/P_∞
	Material	Thickness, t, cm	Temperature, K	Material	Mass, m, g	Velocity, V, km/sec					
1728	Vanadium	0.460	977	Pyrex	0.0160	7.44	0.460	0.355	0.318	Perforation	1.32
1739		.490			.0159	7.26	.490		.346	Perforation	1.42
1727		.559			.0161	7.49	.507		.350	Spall	1.60
1730		.800			.0160	7.35	.355		.348	Spall	2.30
1740		.891			.0158	7.35	.355		.346	Large dimple	2.58
1742		1.27			.0160	7.62	.355		.355	Very slight dimple	3.58
1797	Molybdenum TZM	.558	1365		.0164	7.23	.558	.320	.307	Perforation	1.82
1760		.610			.0159	7.56	.340		.318	Spall	1.92
1692		.711			.0159	7.42	.315				2.24
1678		.711			.0160	7.62	.317				2.24
1679		.776			.0160	7.70	.338				2.45
1677		.925			.0160	7.65	.315				2.91
1681		1.01			.0158	7.78	.305		.320	Dimple	3.15
1680		1.133			.0159	7.78	.320		.320	None	3.54
1783	Titanium - 6-aluminum - 4-vanadium	.416	699		.0164	7.69	.416	.323	.323	Perforation	1.29
1785		.518			.0160	7.69	.518		.320	Perforation	1.60
1784		.567			.0162	7.84	.432		.325	Spall	1.79
1786		.617			.0163	7.84	.388		.325	Spall	1.90
1787		.767			.0164	7.50	.330		.318	Spall	2.42
1798		.957			.0167	7.56	.330		.320	Slight dimple	3.00
1799		3.14			.0165	7.69	.323		.323	None	9.74
1298	316-Stainless steel	.419	294	Nylon	.0189	7.46	.419	.262	.257	Perforation	1.63
1297		.445			.0189	7.44	.310		.257	Spall	1.73
1264		.516			.0190	7.44	.285		.257	Spall	2.01
1263		.549			.0195	7.44	.272		.259	Slight spall	2.11
1197		.584			.0195	7.25	.292		.254	Dimple	2.30
1199		.635			.0189	6.99	.242		.246	Dimple	2.59
1078		.684			.0199	7.46	.262		.262	Slight dimple	2.61
1309		.419		Inlyte	.0196	7.60	.419	.234	.234	Perforation	1.79
1615		.483			.0196	7.40	.338		.232	Spall	2.08
1530		.508			.0196	7.73	.310		.235	Severe dimple	2.16
1374		.549			.0196	7.90	.246		.236	Dimple	2.32
1373		.586			.0195	7.99	.244		.237	Dimple	2.48
1310		.711			.0197	7.60	.236		.235	Slight dimple	3.03
1311		2.54			.0195	7.60	.234		.234	None	----
1705	0.0456-cm Stainless-steel-clad copper	.500	949	Pyrex	.0159	7.45	.500	.685	.685	Perforation	.730
1707		.566			.0156	7.35	.534	.685	.678	Severe spall	.835
1706		.617			.0158	7.37	.685	.685	.685	Spall	.900
1708	0.094-cm Stainless-steel-clad copper	.503			.0155	7.43	.503	.558	.546	Perforation	.920
1710		.556			.0154	7.33	.584	.558	.538	Spall	1.03
1709		.612			.0161	7.45	.558	.558	.558	Spall	1.09

Impact round number: 1569   1565   1295   1294   1254   1255   1256   1296

(a) Inconel-718 targets impacted at room temperature with 0.238-centimeter-diameter spherical pyrex projectiles.

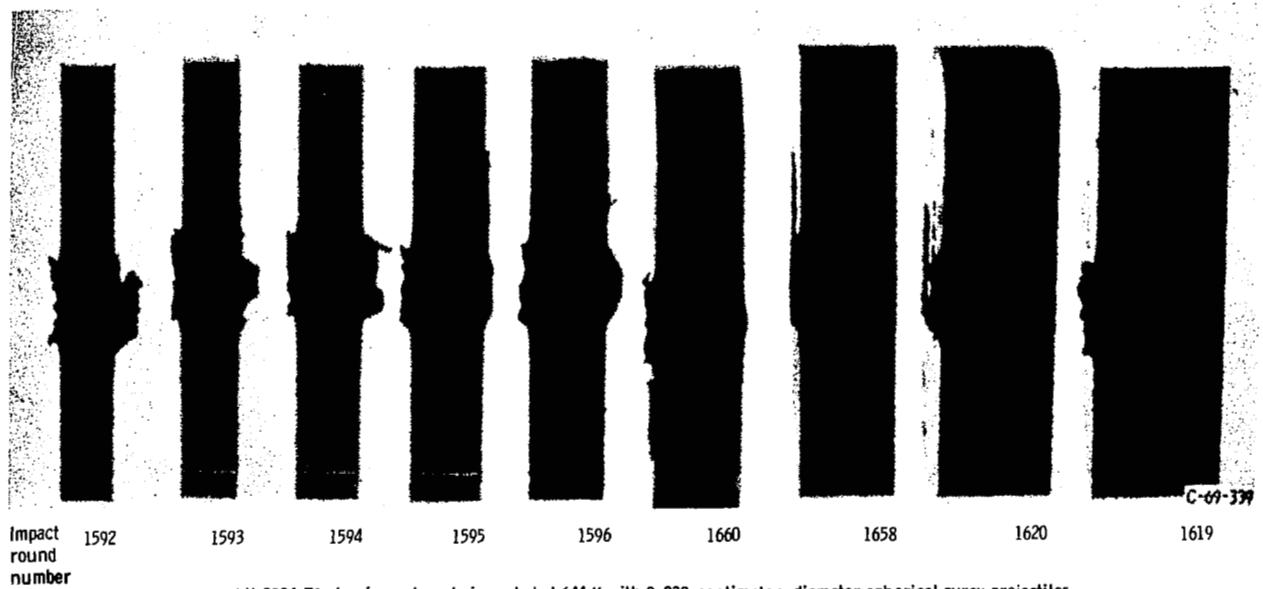Impact round number: 1251   1250   1252   1253   1293
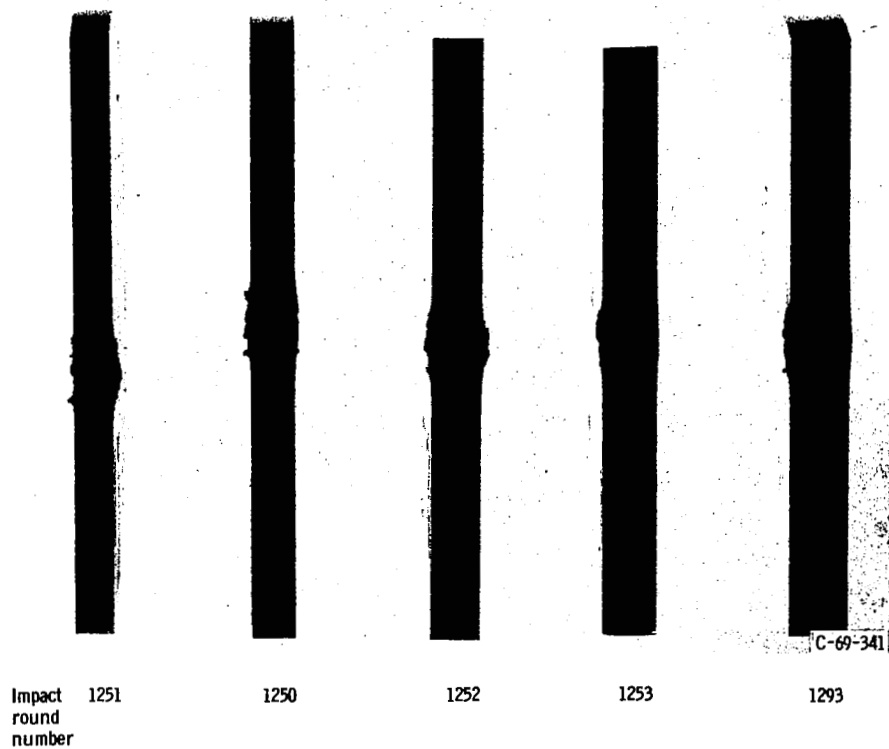
(b) L-605 targets impacted at room temperature with 0.238-centimeter-diameter spherical pyrex projectiles.

Figure 2. – Targets sectioned after impact. Impact velocity, 7.6 kilometers per second.
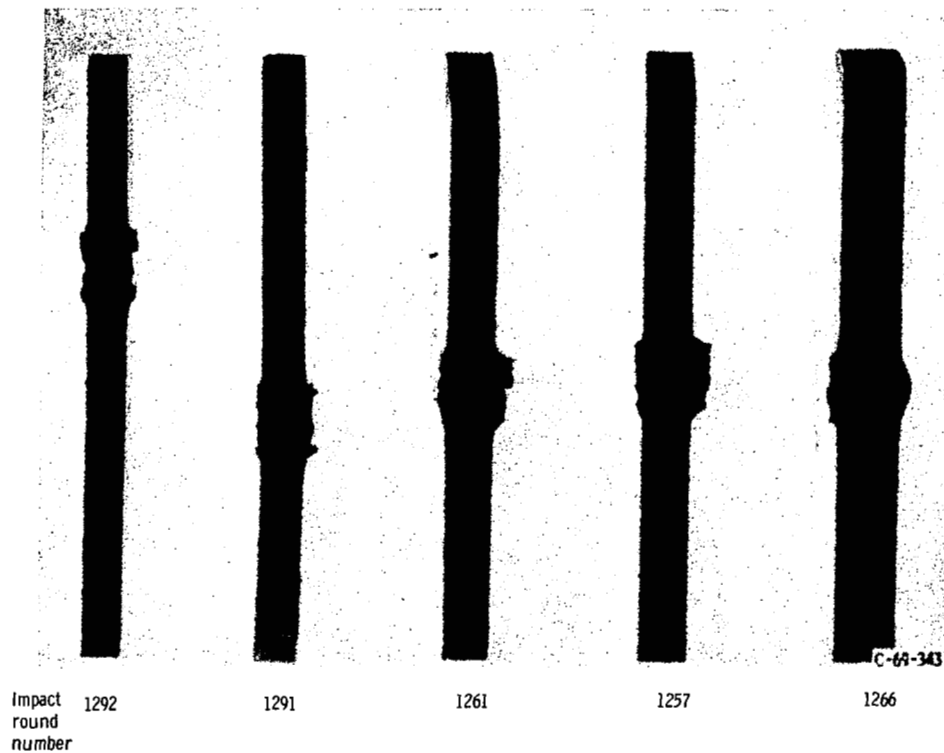
Impact round number   1292   1291   1261   1257   1266

(c) A-286 targets impacted at room temperature with 0.238-centimeter-diameter spherical pyrex projectiles.

Impact round number   1592   1593   1594   1595   1596   1660   1658   1620   1619

(d) 2024-T6 aluminum targets impacted at 644 K with 0.238-centimeter-diameter spherical pyrex projectiles.
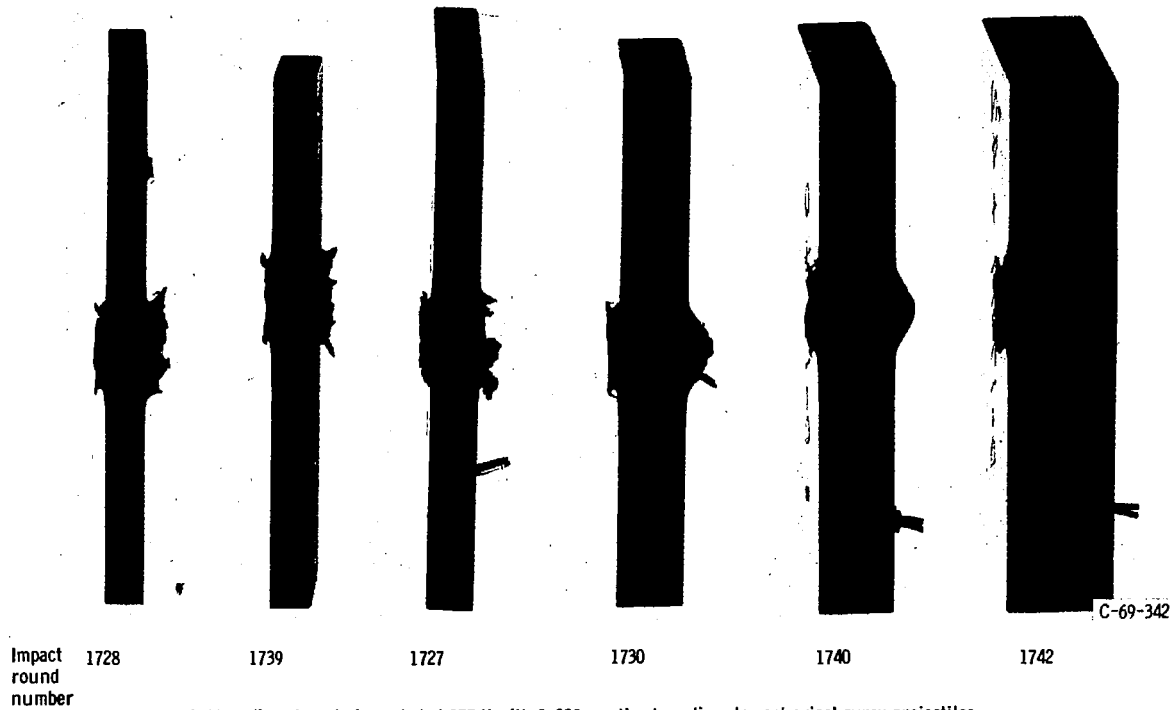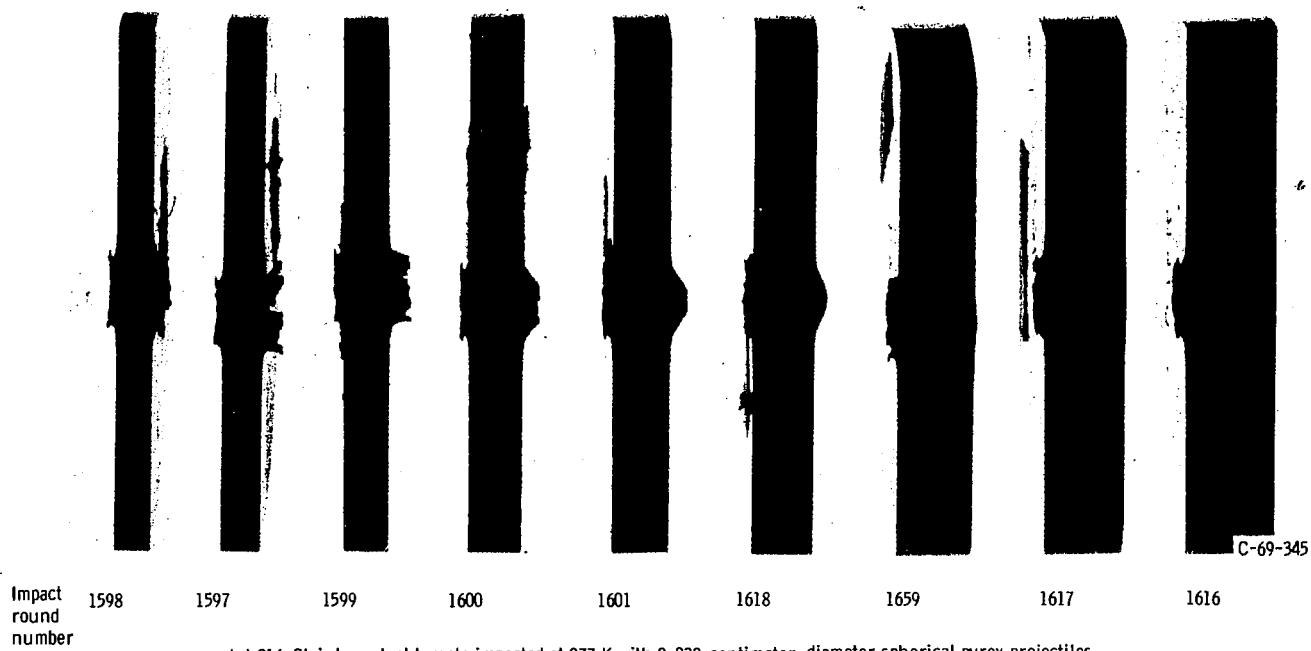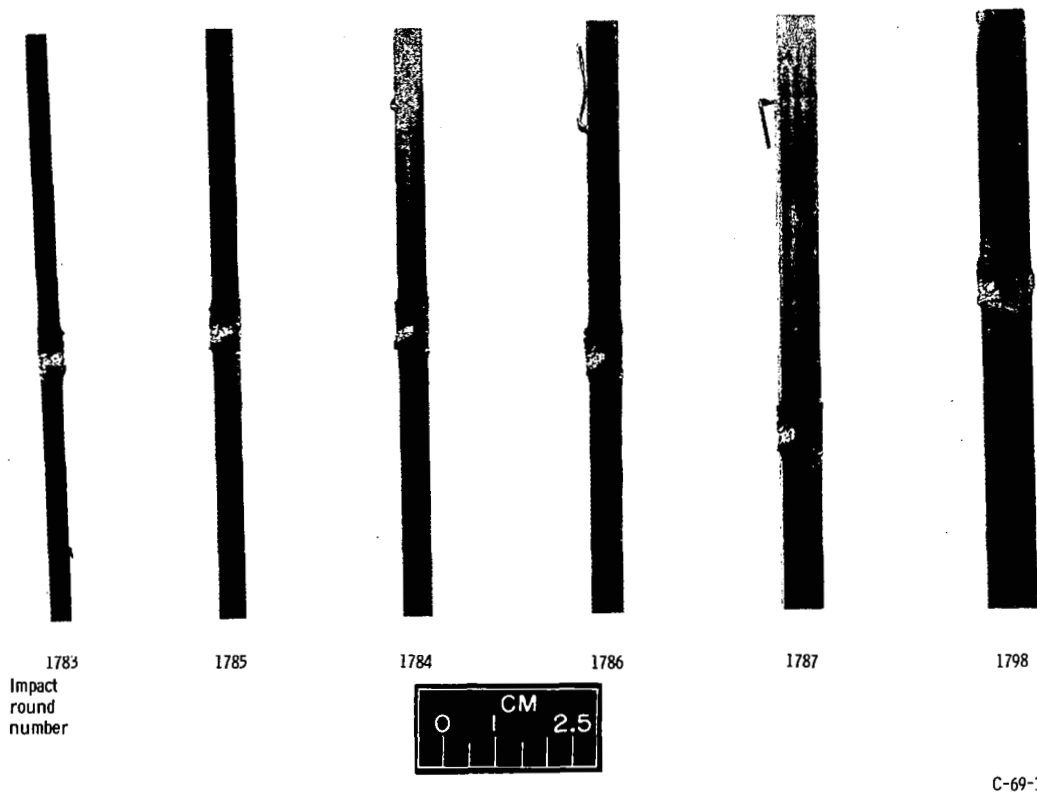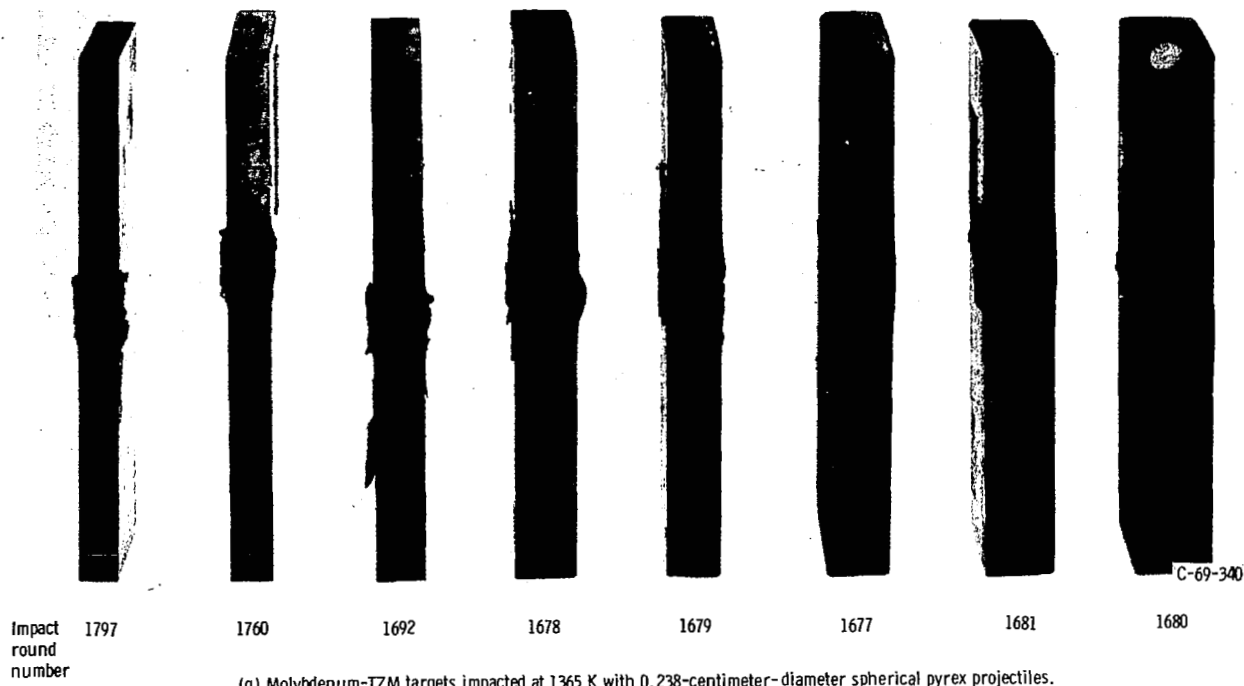
Figure 2. - Continued.

10

Impact round number: 1598   1597   1599   1600   1601   1618   1659   1617   1616

C-69-345

(e) 316-Stainless steel targets impacted at 977 K with 0.238-centimeter-diameter spherical pyrex projectiles.

Impact round number: 1728   1739   1727   1730   1740   1742

C-69-342

(f) Vanadium targets impacted at 977 K with 0.238-centimeter-diameter spherical pyrex projectiles.

Figure 2. - Continued.

11

Impact 1797   1760   1692   1678   1679   1677   1681   1680
round
number

(g) Molybdenum-TZM targets impacted at 1365 K with 0.238-centimeter-diameter spherical pyrex projectiles.

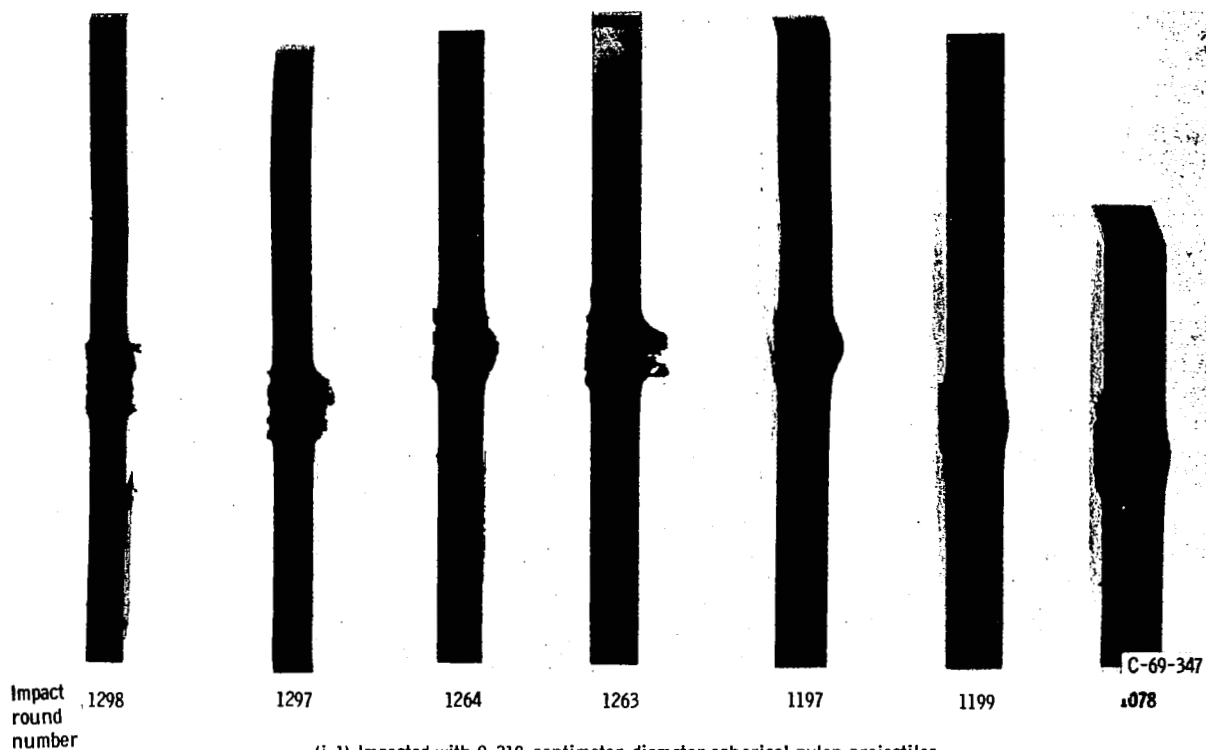1783   1785   1784   1786   1787   1798
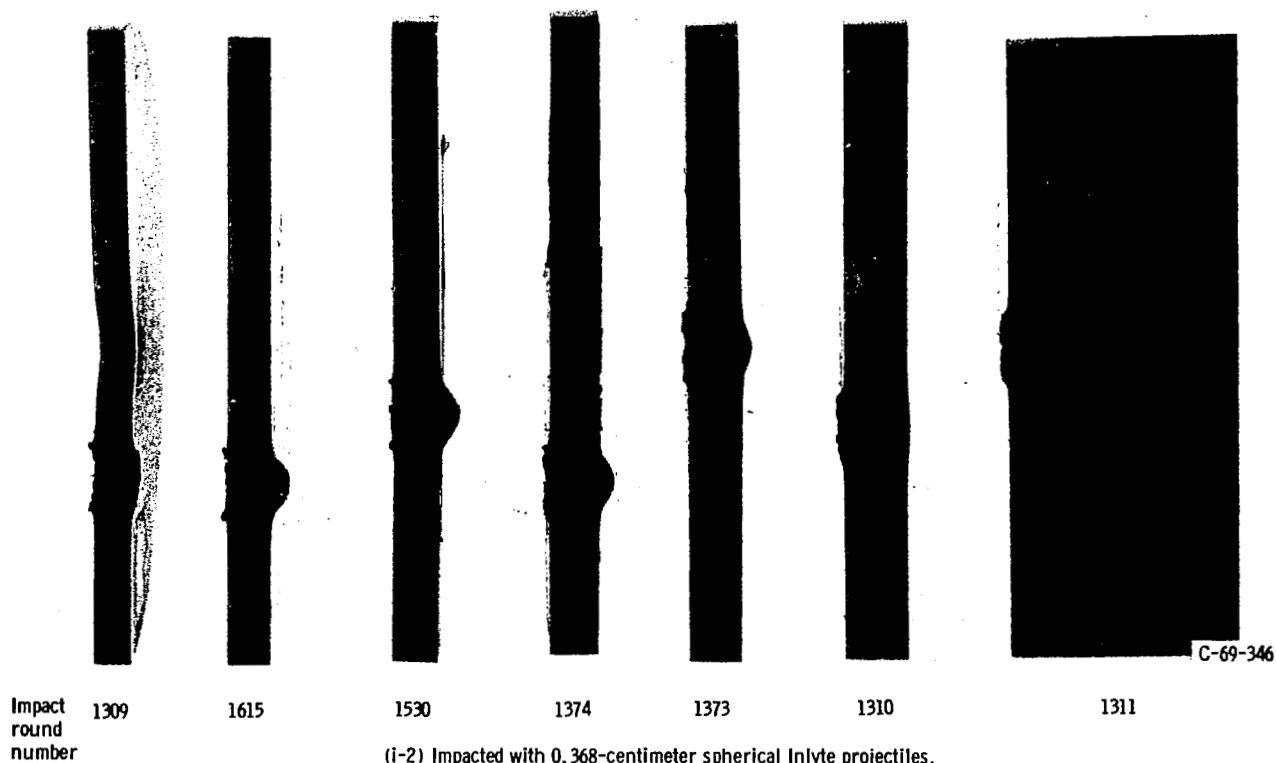Impact
round
number

C-69-3757

(h) Titanium - 6-aluminum - 4-vanadium targets impacted at 699 K with 0.238-centimeter-diameter spherical pyrex projectiles.

Figure 2. - Continued.

12

Impact round number

1298 1297 1264 1263 1197 1199 ı078

C-69-347

(i-1) Impacted with 0.318-centimeter-diameter spherical nylon projectiles.

Impact round number

1309 1615 1530 1374 1373 1310 1311

C-69-346

(i-2) Impacted with 0.368-centimeter spherical Inlyte projectiles.

(i) 316 Stainless steel targets impacted at room temperature.

Figure 2. - Concluded.

13

can be obtained from available correlations of thick-plate penetration depth (e.g., ref. 8).

Values of P_∞ for each test impact were obtained from a single reference value P_∞^* established for each series of tests. The reference value of the semi-infinite penetration depth was taken as the measured value of the penetration depth into the thickest target of each series impacted. These targets, except for the stainless-steel-clad copper, were sufficiently thick (no or very little dimpling) so that the measured penetration depth was equal to the value for a semi-infinite thickness. This reference value, called P_∞^*, was used to calculate a value of P_∞ for each impact in the same series by using the assumption that penetration depth scales with the kinetic energy of the projectile. This assumption has been shown to be quite valid for the range of variation of projectile mass and velocity observed in the tests (refs. 5 to 8). Accordingly, individual values of P_∞ were calculated from the reference value of P_∞^* by the relation

$$P_\infty = P_\infty^* \left(\frac{V}{V^*}\right)^{2/3} \left(\frac{m}{m^*}\right)^{1/3} \tag{1}$$

where V^* and m^* are the values of projectile velocity and mass corresponding to the value of P_∞^*, as measured from the thickest target impacted in each series. This adjusting procedure was necessary because the projectile mass and velocity were not always the same for each impact within a test series. The various calculated values of P_∞ were then used in determining the ratio t/P_∞ for each impact as shown in table II.

Plots of the normalized penetration depth parameter P/P_∞ against normalized target thickness t/P_∞ were made for each material tested as shown in figure 3. The transition points for the regions of perforation, spall, and dimple shown in the figure were estimated by visual observation and comparison of the sectioned targets after impact. For large values of thickness, for which little rear-surface displacements or none is observed, normal thick-target crater characteristics are observed, and P/P_∞ remains equal to 1 (labeled "cratering line"). As dimpling increases, the outward bulging of the rear surface under the point of impact allows the penetration depth to increase causing P/P_∞ to increase. The value of P/P_∞ continues to increase through the spall region until perforation occurs. When perforation occurs, penetration depth is taken equal to the target thickness. Thus, the perforation line is a straight line at 45° on the plots. The point of maximum P/P_∞ corresponds to incipient perforation. The values of target thickness delineating the start of the three damage regions is indicated by the symbol t^*.

Room-temperature impacts. - Impacts at room temperature into Inconel-718, L-605, and A-286 are shown in figures 2(a), (b), and (c), respectively, and the damage region curves for these three materials are shown in figures 3(a), (b), and (c). The damage
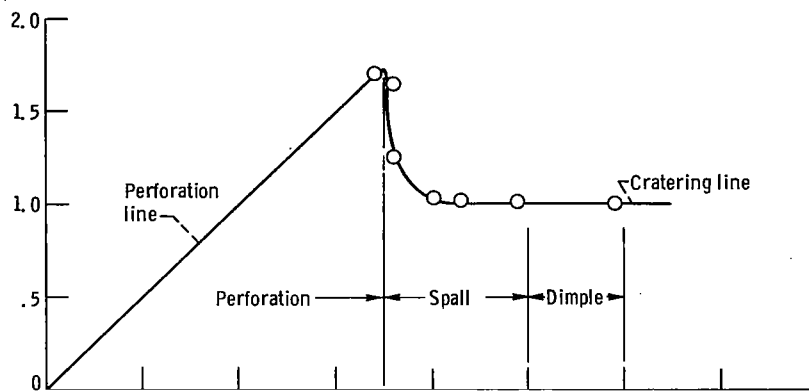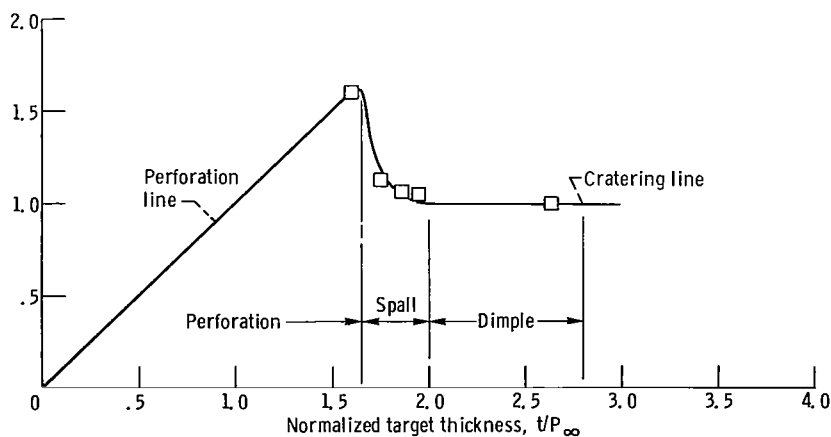
(a) Inconel-718 impacted at room temperature with 0.238-centimeter-diameter pyrex projectiles.
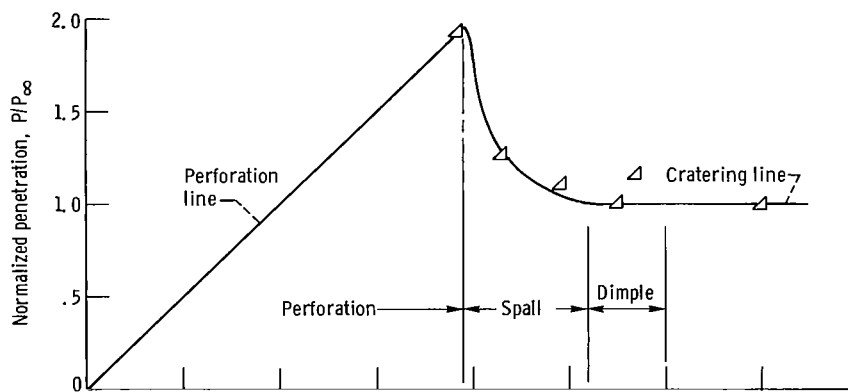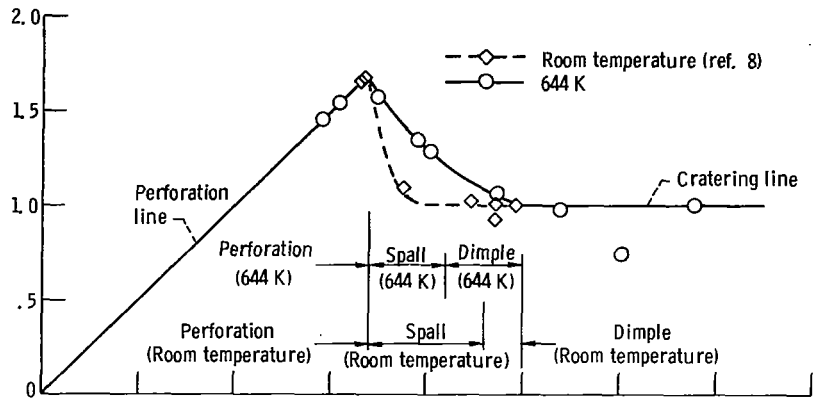

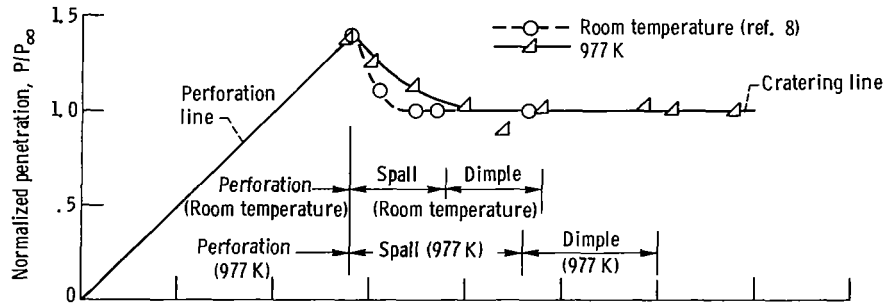(b) L-605 impacted at room temperature with 0.238-centimeter-diameter pyrex projectiles.

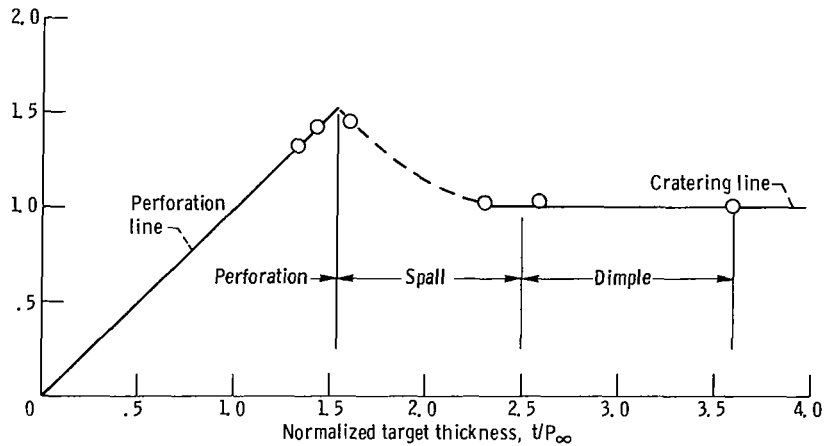(c) A-286 impacted at room temperature with 0.238-centimeter-diameter pyrex projectiles.

Figure 3. - Damage region curves. Impact velocity, 7.6 kilometers per second.

2.0

1.5

--◇-- Room temperature (ref. 8)
--○-- 644 K

Perforation
line ⌐

Cratering line

1.0

Perforation
(644 K)

Spall
(644 K)

Dimple
(644 K)

.5

Perforation
(Room temperature)

Spall
(Room temperature)

Dimple
(Room temperature)

0

(d) 2024-T6 aluminum impacted at 644 K and room temperature with 0.238-centimeter-diameter pyrex projectiles.

1.5

--○-- Room temperature (ref. 8)
--◁-- 977 K

Perforation
line ⌐

⌐Cratering line

1.0

Perforation
(Room temperature)

Spall
(Room temperature)

Dimple

Normalized penetration, P/P∞

.5

Perforation
(977 K)

Spall (977 K)

Dimple
(977 K)

0

(e) 316 Stainless steel impacted at 977 K and room temperature with 0.238-centimeter-diameter pyrex projectiles.

2.0

1.5

Perforation
line ⌐

Cratering line ⌐

1.0

Perforation ⟶

Spall

Dimple

.5

0   .5   1.0   1.5   2.0   2.5   3.0   3.5   4.0

Normalized target thickness, t/P∞

(f) Flat plates of vanadium impacted at 977 K with 0.238-centimeter-diameter pyrex projectiles.

Figure 3. - Continued.

16

(g) Molybdenum-TZM impacted at 1365 K with 0.238-centimeter-diameter pyrex projectiles.

(h) Titanium - 6-aluminum - 4-vanadium alloy impacted at 699 K with 0.238-centimeter-diameter pyrex projectiles.

(i) Flat plates of 316 stainless steel impacted at room temperature with nylon, pyrex, and Inlyte projectiles of approximately equal masses.
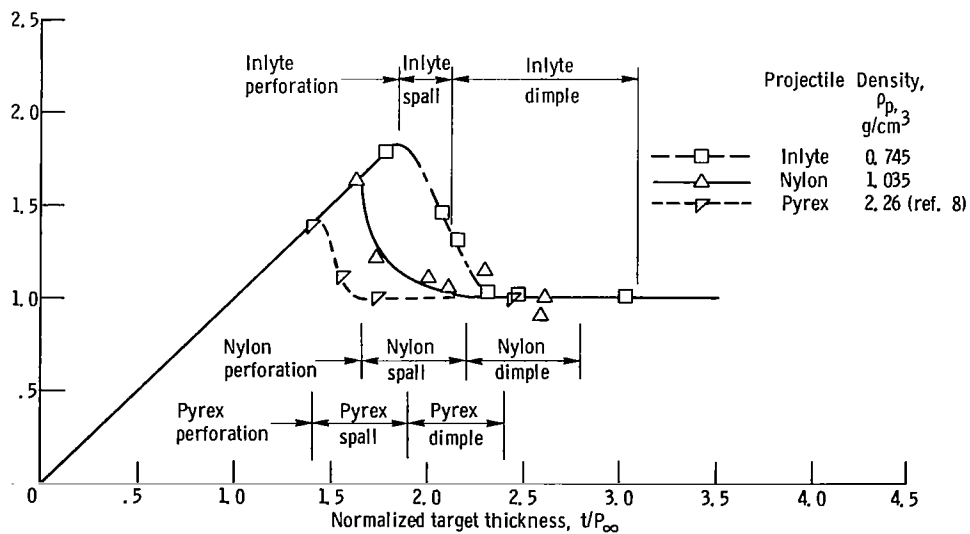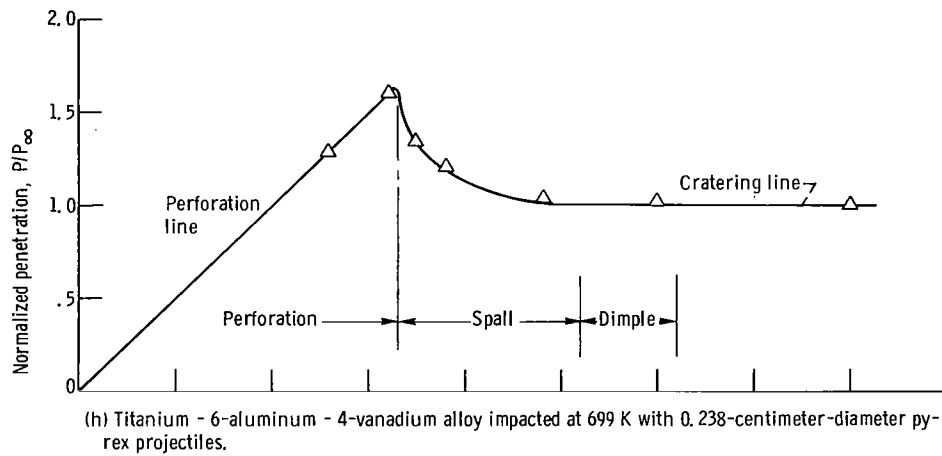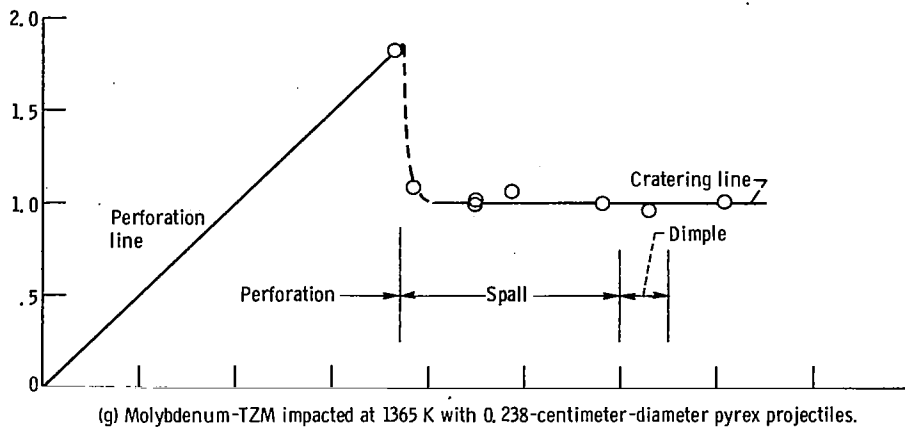
Figure 3. - Concluded.

17

thickness factors at perforation are 1.75, 1.95, and 1.65 for Inconel, L-605, and A-286, respectively. Similarly, t^*/P_∞ at spall is 2.5, 2.6, and 2.0 for Inconel, L-605, and A-286. At dimple, the damage factors are 3.0 for Inconel and L-605 and 2.8 for A-286. Comparison of these damage factors indicates a variation among materials and damage modes. Differences in damage factors between 10 and 40 percent were observed for these conditions of impact, which essentially confirms the conclusions of reference 8 that the damage factors for dimple, spall, and perforation are unique to a particular material.

Elevated-temperature impacts. - The effects of temperature on the damage thickness factors were studied for a series of impacts into 2024-T6 aluminum and 316 stainless steel at 644 and 977 K, respectively. The sectioned targets after impact for both materials are shown in figures 2(d) and (e), and the damage region curves are shown in figures 3(d) and (e).

Figure 3(d) compares the damage region curves for the 2024-T6 aluminum at room temperature and 644 K. The room-temperature data are reproduced from reference 8. The damage factors at both perforation and incipient dimple appear to be the same for both room temperature and 644 K. Thickness at perforation is about 1.7 P_∞ and at dimple about 2.5 P_∞ for both series of impacts. The spall damage factors appear to differ slightly, with the thickness at spall for room-temperature targets at about 2.3 P_∞ and at about 2.1 P_∞ at 644 K. The most noticeable difference in the two curves is that in the 644 K impacts, the crater depth remained greater than P_∞ until dimpling was entirely suppressed. This is not surprising since the material exhibits a more plastic behavior at elevated temperatures.

Figure 3(e) compares the impacts into 316 stainless steel at 977 K with the room-temperature data for 316 stainless steel from reference 8. As in the aluminum targets, the thicknesses at perforation for both series of impacts appear the same at approximately 1.4 P_∞. However, both the spall and dimple regions were extended for the 977 K impacts compared with impacts at room temperature. For the 977 K steel targets, the points of incipient spall and dimple are approximately 2.3 and 3.0 P_∞, respectively, compared with 1.9 and 2.4 P_∞ for the onset of spall and dimple in the room-temperature targets of the same material. Once again, as in the aluminum, the penetration depth is greater for a greater range of target thickness for the elevated-temperature impacts than for the room-temperature impacts.

This comparison of 316 stainless steel and 2024-T6 aluminum at room and elevated temperatures further demonstrates the unique behavior of materials subjected to impacts by high-velocity projectiles. For the aluminum, it appears that the spall and dimple damage factors remain the same or decrease slightly in the elevated-temperature targets when compared with room-temperature targets, whereas in the steel tested, the opposite trend is apparent. It does appear, however, that the damage factors at perforation for the steel and aluminum tested remain unchanged with temperature, indicating that for

18

these particular conditions, the damage factors at perforation scale with temperature; that is, if P_∞ is known as a function of temperature, the target thickness at perforation for elevated temperatures can be calculated from damage factors determined at room temperatures.

Damage thickness factors were also determined for cast vanadium at 977 K, molybdenum-TZM at 1365 K, and Ti-6Al-4V at 699 K. Figures 2(f), (g), and (h) show the sectioned targets after impact, and figures 3(f), (g), and (h) show the corresponding damage region curves. The damage thickness factors at perforation for these three materials impacted by 0.238-centimeter-diameter spherical pyrex projectiles at approximately 7.6 kilometers per second are 1.55, 1.85, and 1.65 for the vanadium, molybdenum, and titanium, respectively. The factors at spall and dimple are 2.5 and 3.6 for vanadium, 3.0 and 3.25 for molybdenum, and 2.6 and 3.1 for titanium. Comparison of these damage factors indicates, as before, a fairly wide variation among materials and damage modes.

Projectile effects. - The effect of various projectile materials on the damage thickness factors was investigated with a series of impacts into 316 stainless-steel targets. The projectiles used included 0.318-centimeter-diameter nylon spheres and 0.368-centimeter-diameter Inlyte spheres. Inlyte is a closed-cell foamed silicate having a nominal density of 0.745 gram per cubic centimeter; the nylon used had a density of approximately 1.035 grams per cubic centimeter. These impacts were compared with the impacts of 0.238-centimeter-diameter pyrex spheres into 316 stainless steel reported in reference 8. The pyrex spheres had a nominal density of 2.26 grams per cubic centimeter. The targets were impacted at room temperature with an impact velocity of about 7.6 kilometers per second. The projectile masses were all approximately 0.018 gram, as shown in table II.

Figure 2(i) shows the sectioned targets after impact for the nylon and Inlyte impacts, and figure 3(i) compares the plots of P/P_∞ as a function of t/P_∞ for the Inlyte, nylon, and pyrex projectile impacts. An interesting trend is apparent from the figure. The damage factors for perforation, spall, and dimple are seen to increase with decreasing projectile density. At perforation, the damage factors are 1.4, 1.65, and 1.85 for the targets impacted by pyrex, nylon, and Inlyte projectiles, respectively. For spall, the factors are 1.9, 2.2, and 2.1; and for dimple, the factors are approximately 2.4, 2.8, and 3.1.

As shown in table II, the crater depths into the thickest targets impacted were slightly less with decreasing density projectiles. This is expected from previous crater correlations in which penetration depth varies with the projectile density to the 2/3 power for equal-mass projectiles (ref. 6). The damage factor trend is thus in opposition to the crater depth variation. However, it should be noted that the important factor for design purposes for a given hazard is t/d. As indicated previously, the variation of t/d with

projectile density can be deduced from the variation of P_∞ with d and ρ_p, where

$$\frac{t^*}{d} = \left(\frac{P_\infty}{d}\right)\left(\frac{t^*}{P_\infty}\right) \tag{2}$$

Then, with

$$\frac{P_\infty}{d} = K(\rho_p)^{2/3} \tag{3}$$

$$\frac{t^*}{d} = K\rho_p^{2/3}\left(\frac{t^*}{P_\infty}\right) \tag{4}$$

where K is a function of the target material and projectile velocity.

If the results of the pyrex impacts are taken as the reference case, then, for the other densities,

$$\frac{\dfrac{t^*}{d}}{\left(\dfrac{t^*}{d}\right)_{pyrex}} = \left[\frac{\rho_p}{(\rho_p)_{pyrex}}\right]^{2/3} \frac{\dfrac{t^*}{P_\infty}}{\left(\dfrac{t^*}{P_\infty}\right)_{pyrex}} \tag{5}$$

The calculated values of damage thickness ratio, as given by equation (5), are listed in table III. Based on projectile diameter, the damage thickness ratio does indeed decrease with decreasing projectile density. The values also suggest that the variation of damage thickness ratio for the damage modes considered is small for a particular density projectile and target material. If this observation is further confirmed, it should lead to

TABLE III. - CALCULATED VALUES OF

DAMAGE THICKNESS RATIOS (EQ. (5))

Projectile		Damage thickness ratio		
Material	Density, g/cm^3	Perforation	Spall	Dimple
Pyrex	2.26	1.0	1.0	1.0
Nylon	1.035	.74	.73	.74
Inlyte	.745	.63	.53	.62

Impact round number

1705   1707   1706   1708   1710   1709
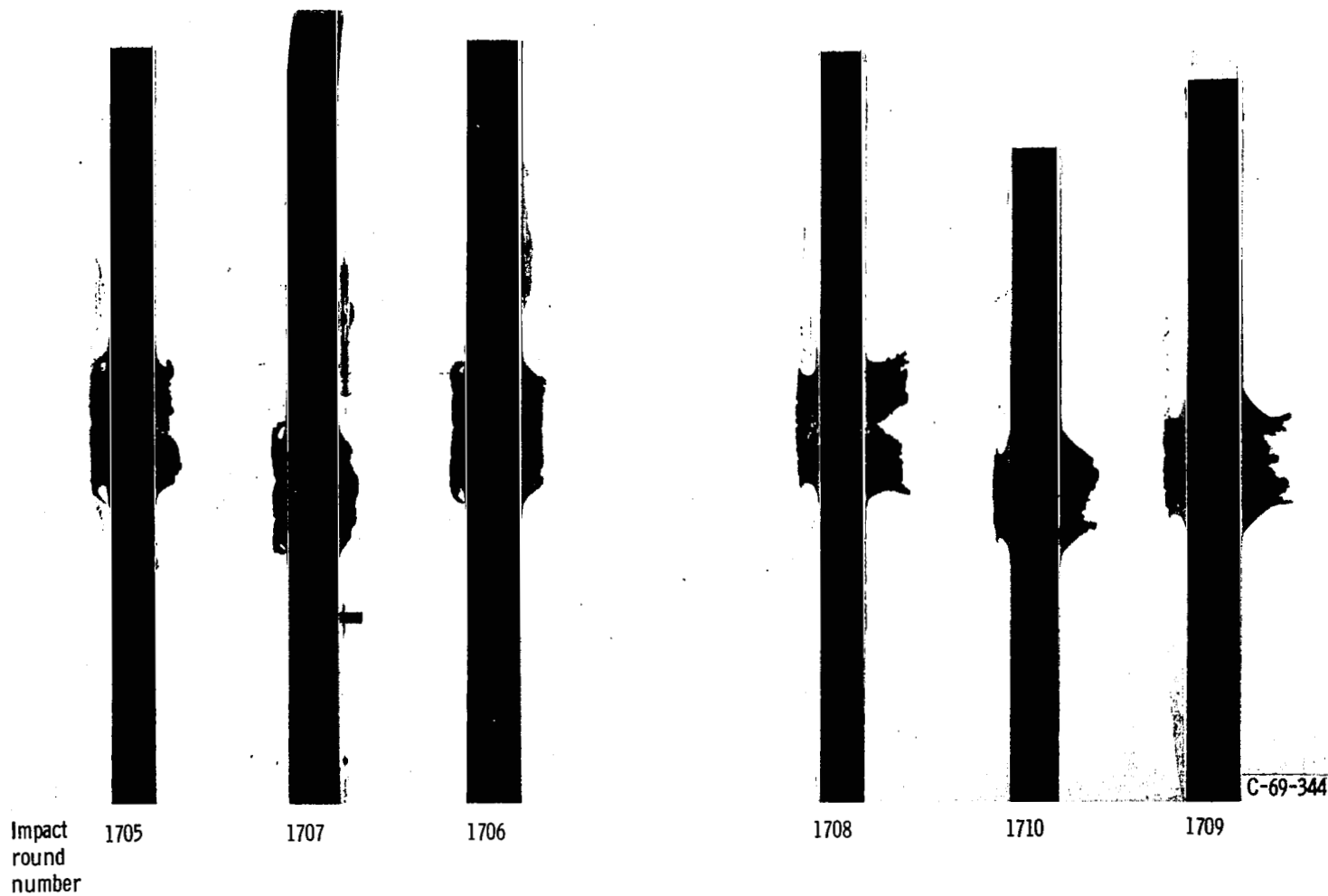
(a) 0.0456-centimeter stainless cladding.   (b) 0.094-centimeter stainless cladding.

Figure 4. - Stainless-steel-clad copper targets sectioned after impact at 949 K with 0.238-centimeter pryex projectiles at 7.6 kilometers per second.

simplification of general damage thickness prediction, in that if a projectile density correlation for one damage mode is determined, the same trends of variation (but not absolute values) should be observed for the other damage modes.

Stainless-clad copper. - As indicated previously, the two stainless-clad copper designs (same total thickness) were varied in thickness to indicate only perforation. The sectioned targets after impact are shown in figure 4. No damage region curves could be drawn because of the few data points covered; however, incipient perforation conditions have been bracketed.

The damage thickness factor for incipient perforation for these targets was difficult to define because of the difficulty in establishing P_∞ for the composite targets for the small range of total thickness covered. In keeping with the previously defined damage factors, P_∞^* was assumed to be equal to the measured depth of penetration in the thickest targets impacted, so that a damage thickness factor could be determined. However, in both cases, spall was present for the thickest targets, so it is not known to what extent the measured value for P_∞^* represents the true thick-target value.

For the thin stainless cladding (table II), the target penetration depth was greater than the target thickness for all three thicknesses, giving rise to values of t^*/P_∞ less than 1 for perforation. Target 1707 appears to be very close to incipient perforation with a damage thickness factor t^*/P_∞ no greater than 0.83. For the thicker stainless cladding (table II), it appears that the thickness at perforation is somewhere around 1.0 P_∞.

These preliminary results of impacts into the clad material might at first indicate a significant reduction in perforation thickness factor compared with the other materials tested, as well as a significant difference between the two clad thicknesses used. However, this is not at all apparent when the corresponding values of t^*/d at perforation are considered. These values are 2.36 and 2.27, respectively, for the 0.0456- and the 0.094-centimeter clad thicknesses.

Comparisons

The various damage factors determined for the nine different flat-plate materials tested, as well as the values determined in reference 8, are summarized in table IV. Even for a given temperature, a wide variation in values of rear-surface damage factor is indicated for the materials tested. The only apparent potential trend is that of an increase in damage factor with increasing target temperature. A comparable wide spread was observed in the relative variations of dimple and spall damage factors compared with the values for perforation, as shown in table V. Here too, there is no completely consistent or uniform pattern, as had been hoped for earlier in the discussion of projectile

TABLE IV. - DAMAGE THICKNESS FACTORS

Material	Temperature, K	Projectile		Rear-surface damage factors					
		Material	Diameter, cm	Dimple		Spall		Perforation	
				t^*/P_∞	t^*/d	t^*/P_∞	t^*/d	t^*/P_∞	t^*/d
316 Stainless steel	[a]$\approx$294	Inlyte	0.368	3.1	1.97	2.6	1.65	1.85	1.17
		Nylon	.318	2.8	2.31	2.2	1.81	1.65	1.36
[b]316 Stainless steel		Pyrex	.238	2.35	3.25	1.9	2.62	1.4	1.93
[b]Columbium - 1-percent zirconium			.318	4.5	6.06	4.0	5.4	1.7	2.29
Inconel 718			.238	3.0	3.42	2.5	2.86	1.75	2.0
L-605				3.0	2.95	2.6	2.56	1.95	1.92
A-286				2.8	3.58	2.0	2.56	1.65	2.10
[b]2024-T6 aluminum				2.5	5.45	2.3	5.01	1.7	3.7
2024-T6 aluminum	644			2.5	6.7	2.1	5.62	1.7	4.55
Titanium - 6-aluminum - 4-vanadium	699			3.1	4.21	2.6	3.53	1.65	2.24
0.0456-cm stainless-steel-clad copper	949			---	----	---	----	.83	2.39
0.094-cm stainless-steel-clad copper	949			---	----	---	----	1.0	2.34
316 Stainless steel	977			3.0	4.44	2.3	3.42	1.4	2.1
Vanadium	977			3.6	5.36	2.5	3.72	1.55	2.31
Molybdenum-TZM	1365			3.25	4.37	3.0	4.03	1.85	2.49

[a]Room temperature.
[b]Ref. 8.

effects. The problem now remains to investigate possible ways for correlating the observed data.

Damage Thickness Correlations

An attempt to correlate the limited rear-surface damage data given in table III was made based on the existing correlating equation for crater depth,

$$\frac{P_\infty}{d} = \gamma \left(\frac{\rho_p}{\rho_t}\right)^{2/3} \left[\frac{V}{\sqrt{\left(\frac{E_t}{\rho}\right)_t}}\right]^{2/3} \tag{6}$$

TABLE V. - RELATIVE THICKNESS RATIOS

| Material | Temperature, K | Damage thickness ratios | |
		$\dfrac{\text{Dimple}}{\text{Perforation}}$	$\dfrac{\text{Spall}}{\text{Perforation}}$
316 Stainless steel	[a]≈294	1.68	1.41
316 Stainless steel		1.70	1.33
[b]316 Stainless steel		1.68	1.36
[b]Columbium - 1-percent zirconium		2.64	2.35
Inconel 718		1.71	1.43
L-605		1.54	1.33
A-286		1.70	1.22
[b]2024-T6 aluminum		1.47	1.35
2024-T6 aluminum	644	1.48	1.26
Titanium - 6-aluminum - 4-vanadium	699	1.88	1.57
316 Stainless steel	977	2.12	1.64
Vanadium	977	2.32	1.62
Molybdenum-TZM	1365	1.75	1.60

[a]Room temperature.
[b]Ref. 8.

which, with equation (2), yields

$$
\frac{t^*}{d} = \gamma \left(\frac{t^*}{P_\infty} \right) \left\{ \left(\frac{\rho_p}{\rho_t} \right)^{2/3} \left[\frac{V}{\sqrt{\left(\frac{E_t}{\rho} \right)_t}} \right]^{2/3} \right\} \tag{7}
$$

Values of $\gamma(t^*/P_\infty)$ were determined for each material in table IV at conditions of incipient dimple, spall, and perforation, based on values of γ obtained from the data of reference 6. Results indicated no essentially constant value of $\gamma(t^*/P_\infty)$ for any of the damage modes. Therefore, it was concluded that the quantity within the braces in equation (7) cannot be used as a general correlating parameter for the three damage thicknesses of interest.

Room-temperature perforation. - Reported in reference 10 by Fish and Summers is a preliminary correlation of target thickness at perforation based on target density and percent elongation, and on projectile velocity. The correlation can be represented by the equation

$$\frac{t^*}{d} = K_1 \left(\frac{1}{\rho_t}\right)^{1/2} \left(\frac{1}{\epsilon_t}\right)^{1/18} V \qquad (8)$$

where t^* is the target thickness at perforation, ρ_t is the target density, ϵ_t is the target material percent elongation, V is the projectile velocity, and d is the projectile diameter.

The targets tested and reported in reference 10 included a wide range of material densities and ductilities and were all impacted at room temperature over a range of velocities from around 2 to more than 6 kilometers per second with 0.0159-centimeter-diameter spherical 2017-T4 aluminum projectiles. Since reference 10 used one type of projectile to impact all targets, no correlation with projectile properties was possible.

The perforation thicknesses reported herein can be correlated with a modified form of equation (8). Reference 8 indicated that target and projectile densities appeared to the same power in cratering correlations. Thus, it was assumed that the ratio $(\rho_p/\rho_t)^{1/2}$ could be substituted in equation (8) for $(1/\rho_t)^{1/2}$ to yield

$$\frac{t^*}{d} = K_2 \left[\left(\frac{\rho_p}{\rho_t}\right)^{1/2} \left(\frac{1}{\epsilon_t}\right)^{1/18} V\right] \qquad (9)$$

where the term in the brackets represents a tentative correlating parameter for perforation. The various values of percent elongation, density, and velocity used in equation (9) for each material along with the calculated values of the parameter are given in table VI. The various values of target density and percent elongation were obtained from

TABLE VI. - DATA FOR PERFORATION CORRELATION

Target material	Target density, ρ_t, g/cm^3	Thickness at perforation, t^*_{cm}	Projectile diameter, d, cm	Ratio at perforation, t^*/d	Projectile density, ρ_p, g/cm^3	Impact velocity, V, km/sec	Target material elongation, ϵ_t, percent	Parameter of eq. (9)
[a]316 Stainless steel	8.0	0.460	0.238	1.93	2.26	7.62	40	3.30
316 Stainless steel	8.0	.432	.318	1.36	1.035	7.46	40	2.19
316 Stainless steel	8.0	.432	.368	1.17	.745	7.60	40	1.89
A-286	7.92	.501	.238	2.11	2.26	7.48	18	3.39
L-605	9.12	.456		1.92		7.16	35	2.92
Inconel-718	8.20	.476		2.0		7.56	5	3.63
[a]2024-T6 aluminum	2.79	.829		3.48		7.62	7	6.22
[a]Columbium - 1-percent	8.05	.736	.318	2.31	2.40	7.62	12	3.60
[a]Zirconium	8.05	.495	.238	2,08	2.26	7.62	12	3.48

[a]Ref. 8.

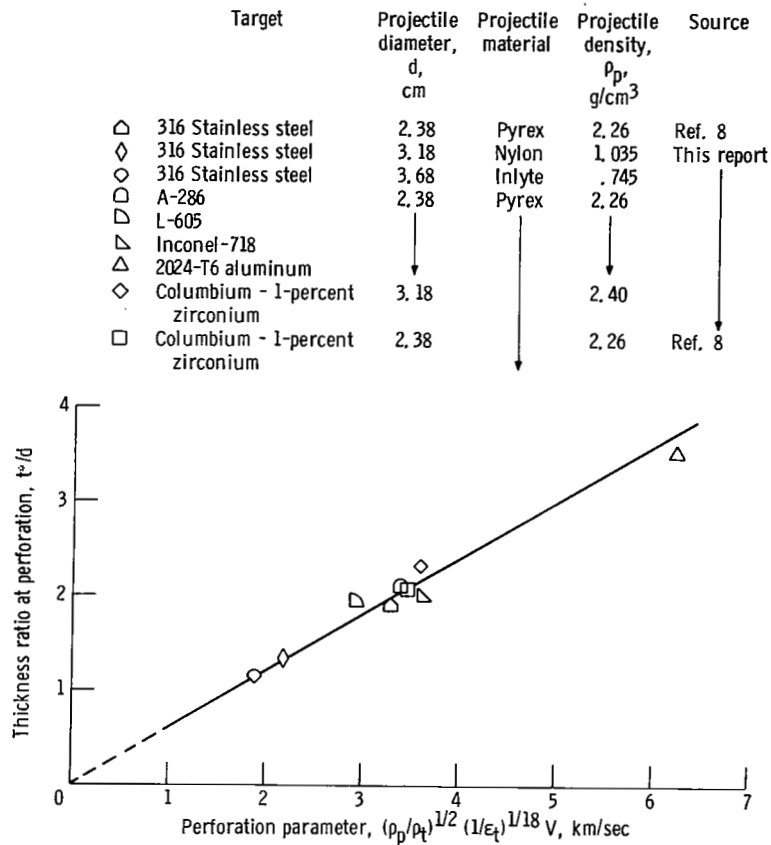|	Target	Projectile diameter, d, cm	Projectile material	Projectile density, ρ_p, g/cm³	Source
△	316 Stainless steel	2.38	Pyrex	2.26	Ref. 8
◇	316 Stainless steel	3.18	Nylon	1.035	This report
○	316 Stainless steel	3.68	Inlyte	.745	
◠	A-286	2.38	Pyrex	2.26	
◠	L-605				
◺	Inconel-718				
△	2024-T6 aluminum				
◇	Columbium - 1-percent zirconium	3.18		2.40	
□	Columbium - 1-percent zirconium	2.38		2.26	Ref. 8

Figure 5. - Correlation of target thicknesses at incipient perforation. Room temperature; impact velocity (nominal), 7.5 kilometers per second.

·unpublished test data on specimens representative of the target materials.

Figure 5 shows a plot of t^*/d against the perforation correlating parameter of equation (9) for the room-temperature perforation points reported in the previous sections for the various target-projectile combinations tested. A straight line can be drawn through the origin and the test points that represents the data very well, thus verifying the assumed density relation of equation (9). Since the impacts reported herein were all nominally at the same velocity, the fit to the data in figure 5 cannot be construed as a confirmation of the linear variation with velocity suggested by reference 10.

The value of K_2 in equation (9) was determined from figure 5 to be 0.6, so that equation (9) becomes

$$\frac{t^*}{d} = 0.6\left[\left(\frac{\rho_p}{\rho_t}\right)^{1/2}\left(\frac{1}{\epsilon_t}\right)^{1/18} V\right] \tag{10}$$

26

where V is in kilometers per second, and ϵ_t is in percent. Equation (10) represents a tentative equation for perforation thickness of plates at room temperature. However, further verification of the velocity exponent is required.

Perforation at elevated temperature. - As stated previously, equation (10) was specifically developed from impacts into targets at room temperature. Examination of the data presented in table IV indicates that the values of t^*/d at perforation vary with temperature. However, figures 3(d) and (e) indicate that the values of t^*/P_∞ at perforation remain constant with temperature. Thus, if P_∞/d can be predicted at elevated temperatures, it should, in principle, be possible to predict the values of t^*/d at elevated temperatures.

Recent results in reference 6 have demonstrated that it is possible to estimate elevated-temperature penetration depths from knowledge of room-temperature values according to the relation

$$\left(\frac{P_\infty}{d}\right)_T = \left(\frac{P_\infty}{d}\right)_R \left(\frac{T}{T_R}\right)^{1/6} \tag{11}$$

where T is the absolute target temperature and T_R is the absolute room temperature. (Subscripts T and R refer to elevated temperature and room temperature, respectively.) Equation (11) was indicated to be limited to ratios of temperature to material melting temperature below 0.7. In principle then, since

$$\left(\frac{t^*}{d}\right)_T = \left(\frac{t^*}{P_\infty}\right)_T \left(\frac{P_\infty}{d}\right)_T \tag{12}$$

and at incipient perforation

$$\left(\frac{t^*}{P_\infty}\right)_T = \left(\frac{t^*}{P_\infty}\right)_R \tag{13}$$

equation (11) can be expressed as

$$\left(\frac{t^*}{d}\right)_T = \left(\frac{t^*}{d}\right)_R \left(\frac{T}{T_R}\right)^{1/6} \tag{14}$$

27

TABLE VII. - COMPARISON OF MEASURED AND CALCULATED VALUES OF

t^*/d AT ROOM AND ELEVATED TEMPERATURES

Material	Temperature, K	Measured t^*/d at room temperature	t^*/d at elevated temperature	
			Measured	Calculated
316 Stainless steel	977	1.935	2.1	2.36
2024-T6 aluminum	644	3.68	4.45	4.20

Equation (14) was checked using the data presented in figures 3(d) and (e) for 2024-T6 aluminum and 316 stainless steel. (These are the only data available for both room- and elevated-temperature perforation thicknesses.) The room-temperature data are from reference 8. The measured values of t^*/d at the elevated temperatures and the values of t^*/d calculated from equation (14) are shown in table VII. The calculated values of the perforation thicknesses are seen to be reasonably close to the measured values, considering the uncertainty involved in determining precise incipient damage thicknesses. However, no firm conclusion as to the general validity of equation (14) for predicting elevated-temperature perforation thicknesses can definitely be made on the basis of these two available data points.

In a further attempt to investigate the validity of equation (14) in estimating perforation thickness at elevated temperature, the elevated-temperature perforation thickness data of table III were corrected to anticipated room-temperature values by use of the factor $(T/T_R)^{1/6}$. A comparison of these values and the prediction of equation (10) is shown in figure 6. The observed comparison together with the values of the previous table.
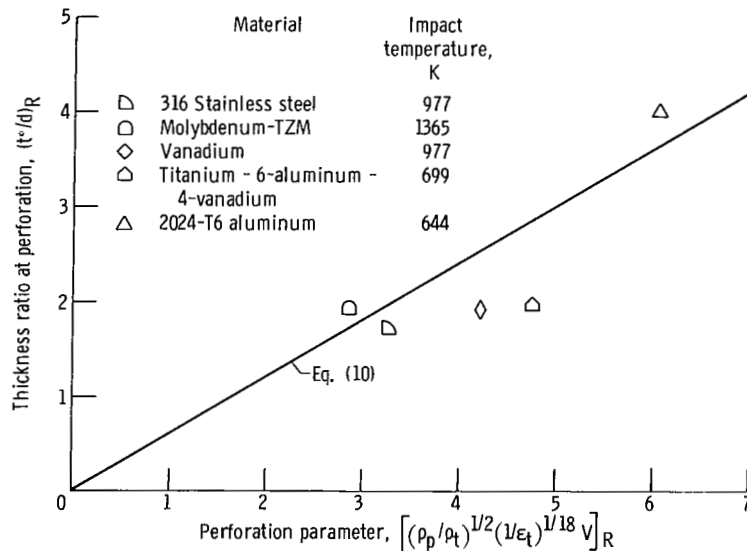

Figure 6. - Comparison of thickness ratio at perforation corrected to room temperature with predicted room-temperature variation.

is interpreted as suggesting a tentative prediction relation for perforation thickness at elevated temperatures existing in terms of room-temperature material properties as

$$\left(\frac{t^*}{d}\right)_T = 0.6\left(\frac{\rho_p}{\rho_t}\right)^{1/2}\left(\frac{1}{\epsilon_t}\right)_R^{1/18} V\left(\frac{T}{T_R}\right)^{1/6} \tag{15}$$

However, it is felt that further elevated-temperature tests are necessary to establish more firmly the effects of operating temperature on required thickness.

Armor Mass

For a practical application, the significant factor is the mass of armor material required to protect against a given damage mode, rather than just the thickness required. An armor mass parameter can be formed from the existing data as the product of target material density and damage factor:

$$M' = \rho_t \frac{t^*}{d} \tag{16}$$

This parameter, in essence, represents a measure of the minimum mass of plate armor required to protect a given surface area against the damage mode of concern.

Calculated values of mass parameter for the three damage modes are listed in table VIII in order of increasing density. A wide range of values is obtained. However, it is recognized that although all tests were conducted at the same nominal impact velocity, the data include variations in target temperature and projectile density. A significant comparison for relative weight should be based on a uniform set of test conditions such as constant target temperature (e.g., room temperature) and constant projectile material (e.g., pyrex). Such a comparison can be obtained for incipient perforation by means of the relation of equation (15). The pyrex equivalent perforation thickness ratio for non-pyrex projectiles was determined from

$$\left(\frac{t^*}{d}\right)_{pyrex} = \left(\frac{\rho_{pyrex}}{\rho}\right)^{1/2}\frac{t^*}{d} \tag{17}$$

and the estimated room-temperature perforation thickness ratio was determined for the

TABLE VIII. - ARMOR MASS PARAMETER (EQ. (16))

Target material	Projectile material	Density, g/cm^3	Temperature, K	Mass parameter, g/cm^3		
				Dimple	Spall	Perforation
2024-T6 aluminum	Pyrex	2.79	[b]≈294	15.2	14.8	9.7
2024-T6 aluminum		2.79	644	18.7	15.7	12.4
Titanium - 6-aluminum - 4-vanadium		4.47	699	18.8	15.8	10.0
Vanadium		6.11	977	32.8	22.8	14.1
A-286		7.92	[b]≈294	28.3	20.3	16.6
316 Stainless steel	Inlyte	8.0		15.8	13.3	9.3
316 Stainless steel	Nylon			18.5	14.5	10.9
[a]316 Stainless steel	Pyrex			26.0	21.0	15.4
316 Stainless steel			977	35.5	27.4	16.8
[a]Columbium - 1-percent zirconium		8.05	[b]≈294	48.8	43.5	18.4
Inconel 718		8.23	[b]≈294	28.2	23.5	16.5
0.094-cm stainless-steel-clad copper		8.6	949	----	----	20.1
0.0456-cm stainless-steel-clad copper		8.7	949	----	----	20.8
L-605		9.15	[b]≈294	27.0	23.4	17.6
Molybdenum-TZM		10.2	1365	44.5	41.1	25.4

[a]Ref. 8.
[b]Room temperature.

elevated-temperature data values from equation (14):

$$\left(\frac{t^*}{d}\right)_R = \left(\frac{T_R}{T}\right)^{1/6} \left(\frac{t^*}{d}\right)_T \tag{18}$$

The resultant tabulation is shown in table IX in order of increasing mass parameter. In general, the armor mass parameter tends to increase with increasing target-material density. The lowest values of mass parameter were obtained for titanium, aluminum, and vanadium. Fortunately, a wide range of design operating temperatures can be covered with these available materials. In addition to design operating temperature, other factors such as cost, fabricability, strength, and compatibility may influence the selection of a suitable lightweight armor material.

At this point, it should be noted that the damage thickness factors and correlations presented herein are values for the onset of the damage mode. Values of armor thickness necessary to prevent a particular damage mode will have to be greater than these values.

TABLE IX. - ARMOR MASS PARAMETER AT

PERFORATION VALUES CORRECTED TO ROOM

TEMPERATURE AND PYREX PROJECTILES

Material	Density, g/cm^3	Mass parameter at perforation, g/cm^3
Titanium - 6-aluminum - 4-vanadium	4.47	[a]8.66
2024-T6 aluminum	2.79	9.7
2024-T6 aluminum	2.79	[a]10.8
Vanadium	6.11	[a]11.6
316 Stainless steel	8.0	[a]13.8
316 Stainless steel		15.4
316 Stainless steel		[b]16.1
316 Stainless steel		[b]16.2
Inconel 718	8.23	16.5
0.094-cm stainless-steel-clad copper	8.6	[a]16.5
0.0456-cm stainless-steel-clad copper	7.92	[a]16.6
A-286	8.7	17.1
L-605	9.15	17.6
Columbium - 1-percent zirconium	8.05	18.4
Molybdenum-TZM	10.2	[a]19.7

[a]Values corrected for target temperature.
[b]Values corrected for projectile density.

However, the amount by which the reported thicknesses should be increased is a matter of design judgement.

SUMMARY OF RESULTS

The following principal results were obtained from an experimental investigation of high-velocity impact damage thickness factors (ratio of target thickness to projectile diameter or to thick-target crater depth) at incipient rear-surface dimple, spall, and perforation for various armor plate materials:

1. Damage thickness factors varied significantly for all three modes of damage, and from material to material. Thickness was greatest at incipient dimple and least at perforation.

2. For almost all materials, the target thickness at perforation was significantly greater than the thick-target (semi-infinite) crater depth due to the outward bulging of the rear surface of the target. The reverse was observed with stainless-steel-clad copper targets.

3. Target thickness at dimple, spall, and perforation increased with increasing target temperature. However, based on the results for stainless steel and aluminum, the ratio of target thickness at perforation to thick-target crater depth remained essentially unchanged.

4. For the three projectile materials tested, a decrease in all three damage factors was observed with a decrease in projectile density.

5. For impacts at room temperature, target thickness at threshold perforation was correlated with the percent elongation and density of the target material and the density of the projectile. A tentative relation for predicting perforation thicknesses in flat plates at elevated temperatures was also presented.

6. Comparison of values of a parameter for mass of armor plate at incipient perforation showed a general tendency for required mass to increase with increasing material density. Lowest values of mass parameter were obtained for aluminum, titanium, and vanadium.

Lewis Research Center,
    National Aeronautics and Space Administration,
       Cleveland, Ohio, October 3, 1969,
          120-27.

REFERENCES

1. Loeffler, I. J.; Lieblein, Seymour; and Clough, Nestor: Meteoroid Protection for Space Radiators. Power Systems for Space Flight. Vol. 11 of Progress in Astronautics and Aeronautics. Morris A. Zipkin and Russell N. Edwards, eds., Academic Press, Inc., 1963, pp. 551-579.

2. Clough, Nestor; and Lieblein, Seymour: Significance of Photographic Meteor Data in The Design of Meteoroid Protection for Large Space Vehicles. NASA TN D-2958, 1965.

3. Bjork, R. L.: Meteoroids vs. Space Vehicles. ARS J., vol. 31, no. 6, June 1961, pp. 803-807.

4. Jaffe, Leonard D.; and Rittenhouse, John B.: Behavior of Materials in Space Environments. ARS J., vol. 32, no. 3, Mar. 1962, pp. 320-346.

5. Eichelberger, R. J.; and Gehring, J. W.: Effects of Meteoroid Impacts in Space Vehicles. ARS J., vol. 32, no. 10, Oct. 1962, pp. 1583-1591.

6. Clough, Nestor; Lieblein, Seymour, and McMillan, A. R.: Crater Characteristics of 11 Metal Alloys Under Hyper-Velocity Impact Including Effects of Projectile Density and Target Temperature. NASA TN D-5135, 1969.

7. Lieblein, Seymour; Clough, Nestor; and McMillan, A. R.: Hypervelocity Impact Damage Characteristics in Armored Space Radiator Tubes. NASA TN D-2472, 1964.

8. Clough, Nestor; McMillan, A. R.; and Lieblein, Seymour: Dimple, Spall, and Perforation Characteristics in Aluminum, Columbium, and Steel Plates Under Hypervelocity Impact. NASA TN D-3468, 1966.

9. Anon.: Aerospace Research Capabilities. Rep. TR63-223, rev., Defense Res. Lab., General Motors Corp., Apr. 1964.

10. Fish, R. H.; and Summers, J. L.: The Effects of Material Properties on Threshold Penetration. Paper presented at the Seventh Hypervelocity Impact Symposium, Tampa, Florida, Nov. 1964.